Atomic Origin of Magnetocrystalline Anisotropy in $Nd_2Fe_{14}B$

D. Haskel,[1] J. C. Lang,[1] Z. Islam,[1] A. Cady,[1] G. Srajer,[1] M. van Veenendaal,[1,2] and P. C. Canfield[3]

[1]*Advanced Photon Source, Argonne National Laboratory, Argonne, Illinois 60439, USA*
[2]*Department of Physics, Northern Illinois University, De Kalb, Illinois 60115, USA*
[3]*Department of Physics and Ames Laboratory, Iowa State University, Ames, Iowa 50011, USA*

(Received 1 August 2005; published 18 November 2005)

The magnetic moment reversal at each of the two inequivalent Nd sites in a single crystal of ferromagnetic $Nd_2Fe_{14}B$ is probed by dichroic resonant diffraction of circularly polarized x rays. The results, supported by theory, show that the c-axis intrinsic magnetic stability of this superior permanent magnetic material arises predominately at one of the Nd sites (g). The other site (f) undermines magnetic stability by favoring a magnetic moment orientation in the basal plane.

DOI: 10.1103/PhysRevLett.95.217207 PACS numbers: 75.25.+z, 75.30.−m, 75.50.Bb

The ability of rare-earth (RE) ions to enhance the stability of modern permanent magnets against demagnetizing fields (coercivity) has resulted in their widespread use in a broad range of products and technologies [1,2]. While earlier steel and ferrite magnets relied mostly on defect-born pinning centers and particle shape anisotropy to achieve significant coercivity, RE ions dramatically enhance coercivity through the interaction of their anisotropic ($4f$) electron clouds with the crystal electric field (CEF) of surrounding charges [3,4]. This interaction together with spin-orbit coupling yields a preferential alignment of the RE magnetic moments along a specific crystalline direction, effectively pinning the moments. The magnetocrystalline anisotropy (MCA) energy involved in disrupting this preferred orientational arrangement provides intrinsic stability against demagnetizing fields, resulting in the higher coercivities of RE-based magnets.

Despite great technological progress, our basic understanding of the atomic origins of MCA in these complex structures is limited. We focus on $Nd_2Fe_{14}B$, the best permanent magnetic material available today. It is well established [4–6] that Nd dominates the MCA energy at ambient temperature, favoring a [001] easy-axis alignment of the magnetization (Fe contributions are at least a factor of 3–4 smaller). However, the simultaneous presence of Nd ions in dissimilar crystalline atomic environments (g and f inequivalent sites of the $P4_2/mnm$ tetragonal space group [7]) has hindered a clear understanding of their role in regulating the intrinsic stability of $Nd_2Fe_{14}B$. In addition to the differing crystal sites, it is difficult to isolate the magnetic response arising solely from the Nd ions due to the overwhelming magnetic background of Fe ions, which provide most of the material's saturation magnetization ($31\mu_B$ for Fe versus $6\mu_B$ for Nd per formula unit [4]). The Fe background also poses a challenge for the interpretation of neutron diffraction measurements of nontrivial Nd moment orientations [8], which is further complicated by the overlap of chemical and magnetic diffraction that occurs in ferromagnetic materials. Element-specific x-ray magnetic circular dichroism (XMCD) measurements partially mitigate this problem by isolating the magnetic responses of RE and TM ions [9], but for most cases this absorption-based technique [10–12] cannot separate the contributions of dissimilar crystalline sites occupied by the same atomic species.

In this Letter, we show that an x-ray scattering approach can be used to measure element- and site-specific magnetic moment reversals by exploiting the symmetry properties of the crystal's space group and the sensitivity of resonant scattering of circularly polarized (CP) radiation to the magnetic moment of the resonant atom. We provide experimental and theoretical evidence that the intrinsic magnetic hardness of $Nd_2Fe_{14}B$ arises predominately from one of the two inequivalent Nd sites. We find that one Nd site (g) strongly prefers the [001] direction at ambient temperature and dictates the macroscopic easy-axis direction. The other Nd site (f) (containing half of all the Nd atoms) reduces the intrinsic stability by favoring alignment along [110]-type directions. The results indicate that coercivity may be enhanced by preferential chemical doping of Nd f sites.

A crystal's space group determines the relative contributions of inequivalent crystal sites to the scattered intensity of each allowed Bragg diffraction peak. Site-specific Nd structure factors $\sum_{n=1}^{4} e^{i\vec{Q}\cdot\vec{r}_n}$, where the sum is over the four *equivalent* Nd sites in the unit cell (f or g Wyckoff sites [7]), $\vec{r}_n$ are their atomic positions, and $\vec{Q}$ are scattering vectors, show that tuning to the (110), (220), and (440) Bragg conditions of a $Nd_2Fe_{14}B$ crystal probes Nd g sites (97%), Nd f sites (96.4%), or weights them almost equally 48.5% and 51.5%, respectively. Element specificity is obtained by tuning the x-ray energy to near the Nd L_2 resonance ($2p_{1/2} \rightarrow 5d$ dipole transition near 6.722 keV), and CP x rays are used to yield magnetic sensitivity [13,14]. The latter arises because the virtually excited, spin-polarized photoelectron is sensitive to the local exchange splitting of Nd $5d$ intermediate resonant states, which is proportional to the Nd $4f$ magnetic moment

[15–17]. A differential measurement of the resonantly scattered intensity for opposite x-ray helicities $I_D = (I^+ - I^-)$ yields magnetic sensitivity, while the sum $I_S = (I^+ + I^-)$ yields chemical sensitivity [18,19]. We define an asymmetry ratio as $AR = I_D/I_S$.

Measurements were done at beam line 4-ID-D of the Advanced Photon Source on a $Nd_2Fe_{14}B$ single crystal grown out of a Nd-rich ternary melt [20,21]. The [110] surface of the crystal was oriented along the scattering vector. An electromagnet delivered a magnetic field (±6 kOe) along the [001] easy-axis direction, which was parallel to the sample surface and in the scattering plane. A piezoelectric-driven diamond (111) phase retarder operated in Bragg transmission geometry [22] was used to convert the x-ray polarization from linear to circular and to switch (1 Hz) between opposite x-ray helicities. The helicity-dependent resonant diffraction was measured through the Nd L_2 resonance using a digital lock-in detection scheme that synchronizes the measured x-ray diffracted intensity with the helicity modulation of the incoming x-ray beam [23]. The Si(111) double-crystal monochromator, phase retarder, and sample's Bragg angles were tracked to maintain their respective diffraction conditions through the resonance energy scans. The XMCD measurements were performed concomitantly by measuring the Nd L_β fluorescence for opposite x-ray helicities using energy-dispersive Si-drift diode detectors. All measurements were done at ambient temperature.

Figures 1(a)–1(c) show resonant chemical (I_S)- and magnetic-sensitive (AR) scattered intensities for the (110), (220), and (440) Bragg reflections in a $Nd_2Fe_{14}B$ crystal magnetically saturated along its macroscopic easy c axis. The AR signal at (110) and (220) Bragg reflections probes Nd magnetism in an element- and site-specific way: There are no magnetic contributions from Fe, since the resonant magnetic scattering amplitude f_m is practically zero away from element-specific resonances, as shown in Fig. 1(d). We recall that the resonantly scattered intensity is given by the modulus square of the structure factor, $|F(Q,E)|^2 = |\sum_n f_n e^{i\vec{Q}\cdot\vec{r}_n}|^2$, with the sum over all atoms in the unit cell. The resonant scattering amplitude is

$$f_n = f_{e,n}(Q,E)(\hat{\epsilon}'^* \cdot \hat{\epsilon}) - i f_{m,n}(E)(\hat{\epsilon}'^* \times \hat{\epsilon}) \cdot \hat{m}_n, \quad (1)$$

where $f_{e,m}$ are complex charge and magnetic scattering amplitudes, $\hat{\epsilon}, \hat{\epsilon}'$ are incident and scattered polarization vectors (complex for circular), and $\hat{m}$ is magnetic moment direction [15]. Since reversing x-ray helicity is equivalent to reversing magnetization direction, adding diffracted intensities for opposite helicities practically measures resonant charge scattering $I_S = |A\sum_n f_{e,n} e^{i\vec{Q}\cdot\vec{r}_n}|^2$ ($f_m^2 \ll f_e^2$), while subtracting these intensities for opposite helicities yields charge-magnetic interference $I_D = -2i\sum_{n,k} A^* B_k f_{e,n}^* f_{m,k} e^{i\vec{Q}\cdot(\vec{r}_n - \vec{r}_k)} + \text{c.c.}$ (A and B polarization factors). An explicit derivation of the angular dependence of I_D (A^*B) for our scattering geometry can be obtained from the density matrix formalism of Blume and Gibbs [24]. With no polarization analysis of the outgoing beam, this yields $(-i/2)[(\hat{k}_i \cdot \hat{m}) + (\hat{k}_f \cdot \hat{m}) \times \cos 2\theta_B]$, with $\hat{k}_{i,f}$ incident and scattered unit wave vectors and θ_B the Bragg angle [25].

For low-Bragg-angle (110) and (220) reflections, this angular dependence can be approximated by $(\hat{k}_i + \hat{k}_f) \cdot \hat{m} = m_z$, where z is along the sample surface and in the scattering plane [inset, Fig. 1(b)]. Magnetic moment reversal

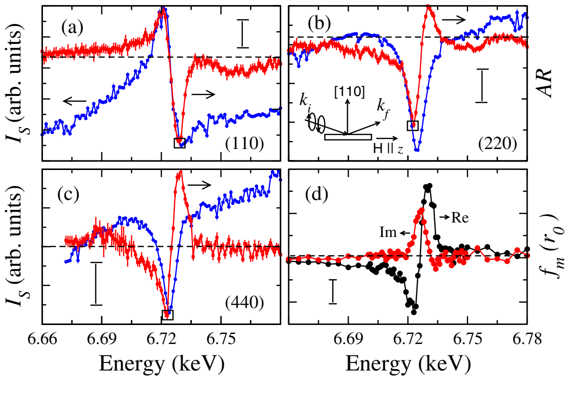

FIG. 1 (color online). (a)–(c) Resonant chemical scattering I_S and magnetic-sensitive resonant scattering AR through the Nd L_2 resonance for selected Bragg reflections. Scale bars for AR are 0.5%. The inset in (b) shows the scattering reflection geometry with k_i and k_f incident and scattered wave vectors, respectively. Squares show energies used for the reversal loops in Fig. 2. (d) Site-averaged, real and imaginary parts of the Nd magnetic resonant scattering amplitude obtained from XMCD (absorption) measurements [31]. Scale bar is 0.2 r_0, with r_0 the classical electron radius.

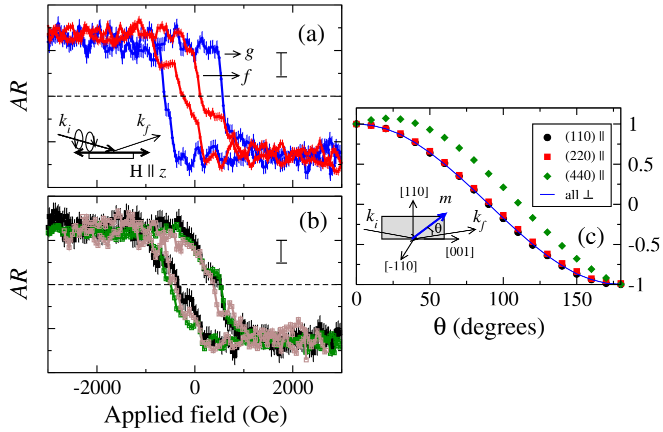

FIG. 2 (color online). (a) Resonant magnetic scattering (AR) loops at (110) and (220) Bragg reflections probing Nd g and f sites, respectively. (b) Site-averaged loops, obtained from absorption XMCD, (440) magnetic scattering, and by averaging the curves in panel (a). Scale bars are 0.5%. (c) Angular dependence of AR for moment rotation parallel (∥) or perpendicular (⊥) to the scattering plane. The angle with the z axis is θ, and values are normalized to those of $\hat{m} \parallel [001]$. The perpendicular case is a $\cos\theta$ dependence for all Bragg reflections.

loops obtained from changes in the *AR* as the strength of an applied magnetic field is varied along *z* are then analogous to conventional magnetization loops with the added element- and site-specific sensitivity.

Moment reversal loops (Fig. 2) were measured for each selected diffraction condition at the resonant energy that maximizes the magnetic signal [shown by squares in Figs. 1(a)–1(c)] [26]. The magnetic response of the inequivalent Nd *f* and *g* sites [Fig. 2(a)] is shown together with site-averaged Nd loops independently determined from (440) resonant diffraction, XMCD (i.e., absorption), and by equally weighting site-specific (110) and (220) loops [Fig. 2(b)]. All loops in Fig. 2 are normalized to match at saturation. The reversal loops shown in Fig. 2(a) clearly indicate a preference for the *g* sites to align with the crystal's *c* axis. Their site-specific loop shows magnetically hard behavior, i.e., high coercivity ($H = -600$ Oe) and full remanence. The reversal to the $-z$ direction is sharp as the moments at *g* sites avoid other crystal orientations. The *f* sites, however, start reversing at very low fields and, in fact, display magnetically soft behavior for $H \parallel c$, i.e., low coercivity and low remanence. As discussed below, this is the result of a hard-axis loop combined with the effect of Fe-Nd exchange, which forces the spins at *f* sites to align with the *c* axis at saturation. The interaction with the crystal electric field, however, does not favor *c*-axis alignment of the spins at *f* sites as derived from these loops and theoretical calculations detailed below. Since the macroscopic easy axis of magnetization is the *c* axis and since Nd dominates the MCA energy in this material at room temperature [4–6], this result alone indicates that Nd *g* sites are predominately responsible for the intrinsic magnetic coercivity of $Nd_2Fe_{14}B$.

The different loops at (110) and (220) diffraction conditions indicate that the relative orientation of Nd *f* and *g* magnetic moments changes with applied field. If their relative orientation remains unchanged within a single magnetic domain, identical loops for Nd *f* and *g* sites are expected as a result of the angular dependence of *AR* [Fig. 2(c)]. This dependence reveals a nontrivial reversal process due to competing anisotropies at inequivalent Nd sites. Since the *AR* scattering signal at the (110) and (220) reflections almost vanishes for $\hat{m} \perp [001]$ [either in the scattering plane or perpendicular to it, Fig. 2(c)], a nearly orthogonal arrangement of magnetic moments at Nd *f* and *g* sites occurs at a reversed applied field $H \sim -200$ Oe. At this field value, the *g* moments remain along $\hat{z}$ due to their stronger coupling to the lattice, while the *f* moments lie in the plane perpendicular to it. This unusual reversal must be accompanied by an inhomogeneous arrangement of Fe moments, as they couple through Fe-Nd and Fe-Fe direct exchange (Nd-Nd coupling is indirect and weak [27]). It is likely that the increased exchange energy of such an inhomogeneous configuration limits the extent of moment rotation at *f* sites past the *xy* plane, introducing a "plateau" in the (220) loops until the delayed reversal of *g* moments takes place. We note that probing the details of Fe reversal with this technique is difficult due to the presence of six inequivalent Fe crystal sites [7].

X-ray penetration depths in excess of microns ensure that the hysteresis loops at (110) and (220) reflections are bulk-sensitive. We can rule out near-surface decomposition or impurity phases being responsible for the measured differences based on identical normalized absorption XMCD loops at (110) and (220) incident Bragg angles and sharp single-crystal diffraction peaks corresponding to the nominal crystal structure of $Nd_2Fe_{14}B$. Since magnetization is probed using selected Bragg peaks, crystalline phase selectivity is inherent in addition to element and site selectivity.

Numerical and analytical calculations of the dependence of the energy on the direction of the Nd magnetic moment are shown in Fig. 3. Numerical calculations for a Nd^{3+} ion include the full Coulomb interaction and the $4f$ spin-orbit coupling. Coulomb parameters obtained in the Hartree-Fock limit were scaled down to 80% to account for screening [28]. The CEF is expanded in spherical tensor operators, $H_{\mathrm{CEF}} = \sum_i B_{kq}(C_q^k)_i$, with B_{kq} CEF parameters [27]. The summation is over the $4f$ electrons. Terms with $k \geq 6$ are important only at lower temperatures and neglected [27,29]. The analytical approach approximates the angular dependence of the anisotropy energy E_{MCA} by taking the expectation value of CEF in the lowest Hund's rule multiplet, $\langle LSJ, M = -J | H_{\mathrm{CEF}} | LSJ, M = -J \rangle$. Racah algebra gives $E_{\mathrm{MCA}} = (K_1 \sin^2\theta + K_2 \sin^4\theta)$, for $\varphi = 45°$ (θ is the angle with the *c* axis; φ is in the *xy* plane). $K_{1,2}$ are obtained from the CEF parameters B_{kq} [27]. A screw axis in the tetragonal $P4_2/mnm$ space group causes a sign change

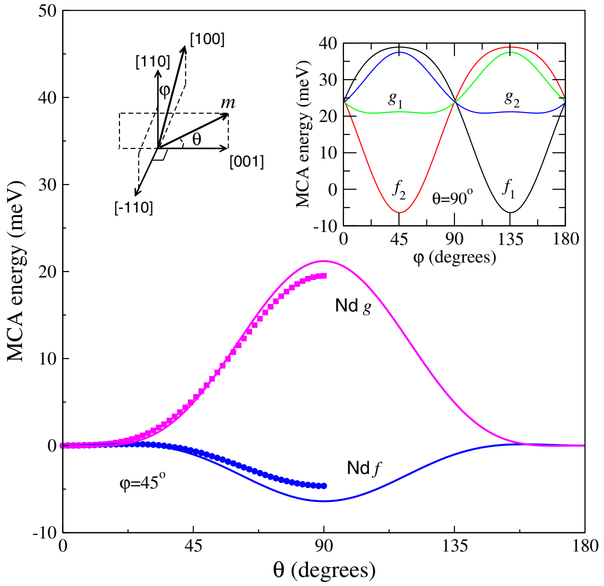

FIG. 3 (color online). The MCA energy for Nd *f* and *g* sites as a function of the angle θ between the magnetic moment direction and the crystal's *c* axis. Points and lines correspond to numerical and analytical calculations, respectively. Inset shows analytical results for moment rotation in the *xy* plane.

of the $B_{n,-2}$ ($n = 2, 4$) for equivalent sites in $z = 0$ and $z = 1/2$ planes, subdividing the sites magnetically into $f_{1,2}$ and $g_{1,2}$.

Figure 3 shows E_{MCA} for the f and g Nd sites as a function of θ at an angle $\varphi = 45°$ with the [100] axis, i.e., in the vertical plane. E_{MCA} of the g sites increases as the moments are forced from the z axis to the xy plane. This result is independent of the in-plane angle φ (inset), showing that the g sites prefer a [001] orientation. However, the f sites favor the xy plane, as their MCA energy is minimized at $\theta = 90°$, with f_1 and f_2 sites preferring $[-110]$ and [110] orientations, respectively (inset). These results clearly strengthen the site-selective z-axis reversal data obtained with magnetic resonant scattering of high coercive squareness for g sites and soft magnetic behavior for f sites.

One might speculate that enhancements of the intrinsic coercivity may be achieved by preferentially substituting at Nd f sites other RE or nonmagnetic ions. Quantitative analysis of the resonantly diffracted intensities shows a significant chemical shift of the absorption threshold between inequivalent Nd sites [30]. This dissimilar local electronic structure may promote preferential substitution. Preferential doping by nonmagnetic ions may increase coercivity by reducing the unwanted contribution of f sites, at the expense of reducing the total saturation magnetization.

In summary, by combining site-specific diffraction with the elemental magnetic fingerprints obtained near atomic resonances, we provide clear evidence that the intrinsic magnetic stability of currently the best permanent magnet $Nd_2Fe_{14}B$ has its atomic origins predominately at the Nd g sites, which strongly prefer c-axis alignment at ambient temperature and dictate the macroscopic easy-axis direction. Chemical substitution at Nd f sites, which undermine stability by favoring the xy plane, may enhance the intrinsic coercivity.

We acknowledge helpful discussion with J. M. D. Coey, A. Berger, and J. S. Jiang. Work at Argonne is supported by the U.S. DOE, Office of Science, under Contract No. W-31-109-ENG-38. M. v. V. is supported by the U.S. DOE Grant No. DE-FG02-03ER46097 and the U.S. Department of Education.

[1] K. H. J. Buschow, in *Handbook on the Physics and Chemistry of Rare Earth*, edited by K. A. Gschneidner, Jr. and L. Eyring (North-Holland, Amsterdam, 1984), Vol. 6, p. 1.
[2] J. M. D. Coey, J. M. Cadogan, and D. H. Ryan, in *Nd-Fe Permanent Magnets: Their Present and Future Applications*, edited by I. V. Mitchell (Elsevier Applied Science, London/New York, 1985), p. 143.
[3] P. Fulde, in *Handbook on the Physics and Chemistry of Rare Earths*, edited by K. A. Gschneidner, Jr. and L. Eyring (North-Holland, Amsterdam, 1979), Chap. 17.
[4] J. F. Herbst, Rev. Mod. Phys. **63**, 819 (1991).
[5] D. Givord, H. S. Li, and R. Perrier de la Bthie, Solid State Commun. **51**, 857 (1984).
[6] M. Bogé *et al.*, Solid State Commun. **55**, 295 (1985).
[7] J. F. Herbst, J. J. Croat, F. E. Pinkerton, and W. B. Yelon, Phys. Rev. B **29**, 4176 (1984).
[8] P. Wolfers, S. Obbade, D. Fruchart, and R. Verhoef, J. Alloys Compd. **242**, 74 (1996).
[9] J. Chaboy *et al.*, Phys. Rev. B **57**, 8424 (1998).
[10] G. Schütz *et al.*, Phys. Rev. Lett. **58**, 737 (1987).
[11] P. Carra and M. Altarelli, Phys. Rev. Lett. **64**, 1286 (1990).
[12] J. Stöhr, J. Magn. Magn. Mater. **200**, 470 (1999).
[13] S. W. Lovesey and S. P. Collins, in *X-Ray Scattering and Absorption by Magnetic Materials* (Clarendon, Oxford, 1996).
[14] H. A. Durr *et al.*, Science **284**, 2166 (1999).
[15] J. P. Hannon, G. T. Trammell, M. Blume, and D. Gibbs, Phys. Rev. Lett. **61**, 1245 (1988).
[16] P. Carra, M. Altarelli, and F. de Bergevin, Phys. Rev. B **40**, 7324 (1989).
[17] J. Miguel-Soriano, J. Chaboy, L. M. Garcia, F. Bartolome, and H. Maruyama, J. Appl. Phys. **87**, 5884 (2000).
[18] F. de Bergevin *et al.*, Phys. Rev. B **46**, 10 772 (1992).
[19] D. Haskel *et al.*, Phys. Rev. Lett. **87**, 207201 (2001); D. Haskel *et al.*, IEEE Trans. Magn. **40**, 2874 (2004).
[20] P. C. Canfield and Z. Fisk, Philos. Mag. B **65**, 1117 (1992).
[21] P. C. Canfield and I. R. Fisher, J. Cryst. Growth **225**, 155 (2001).
[22] K. Hirano, K. Izumi, T. Ishikawa, S. Annaka, and S. Kikuta, Jpn. J. Appl. Phys. **30**, L407 (1991); J. C. Lang and G. Srajer, Rev. Sci. Instrum. **66**, 1540 (1995).
[23] Y. Hayasaki *et al.*, J. Phys. Condens. Matter **16**, 1915 (2004).
[24] M. Blume and D. Gibbs, Phys. Rev. B **37**, 1779 (1988); J. P. Hill and D. F. McMorrow, Acta Crystallogr. Sect. A **52**, 236 (1996).
[25] The $\cos 2\theta$ term was misplaced in Ref. [19].
[26] The normalized field dependence of AR was found to be independent of resonant energy.
[27] M. Yamada, H. Kato, H. Yamamoto, and Y. Nakagawa, Phys. Rev. B **38**, 620 (1988).
[28] R. D. Cowan, in *Theory of Atomic Structure and Spectra* (University of California, Berkeley, 1981).
[29] J. M. Cadogan, J. M. D. Coey, J. P. Gavigan, D. Givord, and H. S. Li, J. Appl. Phys. **61**, 3974 (1987).
[30] D. Haskel *et al.* (to be published).
[31] The optical theorem implies XMCD $\propto \mathrm{Im}(f_m)$. We used tabulated bare-atom scattering factors away from resonance for absolute normalization and a Kramers-Krönig transformation to obtain $\mathrm{Re}(f_m)$.